Cao, X.Y. and Ming, F.R. and Zhang, A.M. and Tao, L. (2018) Multi-phase SPH modelling of air effect on the dynamic flooding of a damaged cabin. Computers and Fluids, 163. pp. 7-19. ISSN 0045-7930 , http://dx.doi.org/10.1016/j.compfluid.2017.12.012

This version is available at https://strathprints.strath.ac.uk/63744/

Multi-phase SPH Modeling of air effect on the dynamic flooding of a damaged cabin

X.Y. Cao[a], F.R. Ming[a], A.M. Zhang[a,*], L. Tao[a,b]

[a] *College of Shipbuilding Engineering, Harbin Engineering University, Harbin 150001, China*

[b] *Department of Naval Architecture, Ocean & Marine Engineering, University of Strathclyde, Glasgow G4 0LZ, UK*

The air flow may take effects on the responses of the damaged ship in the dynamic flooding process. It not only relates to the amount of inflow but also the stability of the ship. In order to accurately predict the responses of a damaged ship, it is essential to take the air into account. In this study, a multi-phase SPH model combined with a dummy boundary method is proposed. One of the advantages of the new SPH model in solving this nonlinear problem is that, it does not rely on other algorithms to track the interface of different phases but can easily deal with breaking, splashing and mixing. The stability and accuracy of the numerical model are verified by comparing with experimental and published numerical results. The air captured in the flooding process is further studied with focus on the exchange of air and water near the opening. Finally, the effects of the sizes and number of the deck openings on the air flow are analyzed. It is found that the air flow can reduce the kinematic energy of inflow water, leading to decreases in the dynamic moment formed by the flooding water and sinking rate of damaged cabin.

Keywords: Flooding; Multi-phase SPH model; Air flow; Dynamic response

---

[*] Corresponding author. E-mail address: zhangaman@hrbeu.edu.cn (A.M. Zhang).

1. Introduction

The flooding of a ship is a complex multiphase flow problem and also a fluid-structure interaction problem[1]. Once the hole is produced on the outer plate, the water may flow into the ship cabin rapidly and impact on the inner structures, meanwhile the air inside the ship will be compressed or pushed out. Due to the large deformation, splashing and breaking of free surface, air bubbles may be trapped in water and coalesced at the interface. Besides, for the rapid flooding case, the air cushion above the water level can be formed in an airtight cabin. What's worse, these complex fluid flows are coupled with the nonlinear motion of the ship hull [2, 3], so it is very difficult to forecast the complicate hydrodynamic process. During the flooding process, the dynamics of the air flow play a dominant role and compromise the stability of the damaged ship, which may lead to severe consequence [4] and warrants thorough study.

Palazzi and De Kat [5] found by experiment that the air flow will introduce additional damping and the air compressibility will cause the energy dissipation, thus the fluid motion and resonance amplitude are restrained. Hearn et al. [6] developed the stiffness expression for the internal air to study the aerostatic influences of the air on the motion of a damaged ship. Different models for the internal air stiffness were proposed to satisfy the adiabatic equation. Smith[7] measured the wave loads of a damaged cabin model under the forced vibration and found that the air increases the motion damping of the model. Ruponen et al. [8-10] pointed that the air flow and air pockets have significant influences on the dynamic flooding process of a damaged cabin in certain conditions by comparative studies of experiment and numerical simulation. Strasser et al. [11] used a CFD code based on RANSE and VOF method to model the flooding considering with air compression, and noticed that flooding in ship without large air ventilations slowed down when the damaged opening was fully submerged. Air flow and

air compression may further complicate the dynamic flooding process. In most studies on the topic reported to date, the flooding water in the cabin is assumed as a flat surface parallel to the sea level, then the dynamic flooding motion and the exchange of the air and water nearby the opening are ignored. However, for a damaged cabin flooding with a high rate or flooding with fluid breaking and coalescing, the assumption can result in a large discrepancy compared to the actual situation. In order to obtain the realistic flooding process, it is necessary that the numerical model for dynamic flooding is applied with the above-mentioned factors being considered properly. The meshless smoothed particle hydrodynamics (SPH) method in solving the dynamic flooding process, which relates to free surface sloshing [12, 13], slamming [14, 15] and coupling with structures [16-18], has shown its distinct advantages. With the development of SPH technique [19-21], the approaches for the interface of different phases [22-24] and computational efficiency [25, 26] have been improved.

To investigate the flooding process considering the air flow, the multi-phase SPH model is developed in this paper. Validated by two benchmarks, i.e., the classical dam-break and the sinking process of an intact box, the multi-phase SPH model is then applied to the comparative study of a damaged cabin flooding with or without air flow to reveal the influencing mechanism. Finally, the dynamic exchange of air and water for the damaged cabin with different openings on the upper deck is studied and the effects of air flow are examined.

2. Numerical methods

2.1. Basic equation of the multi-phase SPH

To solve the dynamic flooding process of interest, a multi-phase model is developed based on SPH model in Colagrossi and Landrini [24], which is a simple procedure to predict the interactions between different phases. The multi-phase SPH model is based on the assumption

of the weakly-compressible fluid and can be solved in an explicit way. The air is assumed to be iso-entropic thus it is not necessary for solving the energy equation and the pressure is the function of density. The Navier-Stokes equations for weakly compressible fluids in a Lagrangian form are as follow:

$$\begin{aligned}
\frac{\mathrm{D}\rho}{\mathrm{D}t} &= -\rho\nabla\cdot\mathbf{v} \\
\frac{\mathrm{D}\mathbf{v}}{\mathrm{D}t} &= \mathbf{g} - \frac{\nabla\mathrm{P}}{\rho} \\
\frac{\mathrm{D}\mathbf{x}}{\mathrm{D}t} &= \mathbf{v} \\
\mathrm{P} &= \mathrm{P}(\rho)
\end{aligned} \tag{1}$$

Where ρ, $\mathbf{v}$, $\mathbf{x}$, $\mathbf{g}$ and P denote the density, the velocity, the coordinate, the gravity acceleration and the pressure, respectively. In order to solve Eq. (1), the derivatives in it can be firstly written as an integral in the domain through the kernel approximation. For a certain vector function $\mathbf{f}(\mathbf{x})$, the divergence can be transformed as [27]

$$<\nabla\cdot\mathbf{f}(\mathbf{x})>\approx\int_{\Omega}\mathbf{f}(\mathbf{x}')\cdot\nabla W(\mathbf{x}-\mathbf{x}')\,\mathrm{d}\,\mathbf{x}' \tag{2}$$

Where $\mathbf{x}'$ is an adjacent position of $\mathbf{x}$ and $W(\mathbf{x}-\mathbf{x}')$ is the kernel function.

When the problem domain is discretized into particles, the particle approximation can be applied to discretize the integral by the weighting summation of neighboring particles in the support domain [27]. For the divergence of a vector function $\nabla\cdot\mathbf{f}(\mathbf{x})$, the approximation at the particle i can be carried out by the neighboring particles j as

$$\nabla_{i}\cdot\mathbf{f}(\mathbf{x})=\int_{\Omega}\mathbf{f}(\mathbf{x}')\cdot\nabla W(\mathbf{x}-\mathbf{x}')\,\mathrm{d}\,\mathbf{x}'=\sum_{j\in\Omega}\mathbf{f}(\mathbf{x}_{j})\cdot\nabla_{i}W_{ij}V_{j} \tag{3}$$

Where W is selected as the renormalized Gaussian kernel function [16, 28]; V is the volume of the particle, which changes with the density in the simulation. Thus, it is easy to obtain that the divergence of a constant vector function is zero. There holds

$$\mathbf{f}(\mathbf{x}_i) \cdot (\nabla_i \cdot \mathbf{1}) = \mathbf{f}(\mathbf{x}_i) \cdot \sum_{j \in \Omega} \nabla_i W_{ij} V_j = \sum_{j \in \Omega} \mathbf{f}(\mathbf{x}_i) \cdot \nabla_i W_{ij} V_j = 0 \tag{4}$$

Thus, the equation in a symmetric form is obtained by subtracting Eq. (4) from Eq. (3)

$$\nabla_i \cdot \mathbf{f}(\mathbf{x}) = \sum_{j \in \Omega} \left[\mathbf{f}(\mathbf{x}_j) - \mathbf{f}(\mathbf{x}_i) \right] \cdot \nabla_i W_{ij} V_j \tag{5}$$

For the gradient of a scalar function $f(\mathbf{x})$, it can be written as

$$\nabla_i f(\mathbf{x}) = \int_\Omega f(\mathbf{x}') \nabla W(\mathbf{x} - \mathbf{x}') d\mathbf{x}' = \sum_{j \in \Omega} f(\mathbf{x}_j) \nabla_i W_{ij} V_j \tag{6}$$

Conducting the similar transformation as Eq. (4), the gradient of the scalar function can be derived as Eq. (7).

$$\nabla_i f(\mathbf{x}) = \sum_{j \in \Omega} \left[f(\mathbf{x}_j) + f(\mathbf{x}_i) \right] \nabla_i W_{ij} V_j \tag{7}$$

It should be underlined that different forms for the gradient of the scalar function and the divergence of the vector function are used. The form of Eq. (7) allows an anti-symmetric property which is crucial for maintaining the momentum conservation when $f(\mathbf{x})$ represents the pressure, while the form of Eq. (5) can decrease the errors introduced by the kernel truncations near the free surface, see more analyses in Colagrossi et al. [29].

Through the transformation of Eq. (5) and Eq. (7), the continuity and momentum equation in Eq. (1) can be expressed as:

$$\frac{D\rho_i}{Dt} = \rho_i \sum_j (\mathbf{v}_i - \mathbf{v}_j) \cdot \nabla_i W_{ij} V_j \tag{8}$$

$$\frac{D\mathbf{v}_i}{Dt} = \mathbf{g} - \sum_j \frac{1}{\rho_i} (P_i + P_j) \nabla_i W_{ij} V_j + \mathbf{f}_v \tag{9}$$

Where the subscripts i and j represent a pair of interacting particles, $\mathbf{g} = (0, -9.81) \, \text{m/s}^2$ and $\mathbf{f}_v$ is the viscous force. In solving the multi-phase flow problem, there exist density differences across the interface of different phases, which may lead to approximation errors of

the particle density so that pressure oscillations usually occur near the interface. In Eqs. (8) and (9), for the pairing particles i and j from different phases, only the volume of the particle from another phase contributes to the approximation but not the density. Also, because the uniform volume is used for different phases at the initial time, so it benefits the smooth approximation of the fields at the interface, e.g., the pressure and the velocity fields.

To solve the Eqs. (8) and (9), the relationship between pressure and density is normally used in SPH method. For the fluid of different phases, the Tait equation [28] improved by Nugent and Posch [30] is adopted:

$$P_w = B[(\frac{\rho_w}{\rho_{w0}})^{\gamma_w} - 1] + P_0$$

$$P_a = B[(\frac{\rho_a}{\rho_{a0}})^{\gamma_a} - 1] + P_0 - \chi\rho_a^2$$

(10)

Where the subscript w represents the heavier phase and a represents the lighter phase. For water: $\gamma_w = 7$, the initial density is $\rho_{w0} = 1000 \text{kg} / \text{m}^3$; while for air: $\gamma_a = 1.4$ [24], and the initial density is $\rho_{a0} = 1.29 \text{kg} / \text{m}^3$. The same coefficient $B = c_a^2 \rho_{a0} / \gamma_a = c_w^2 \rho_{w0} / \gamma_w$ is proposed by Colagrossi and Landrini [24] for ensuring the identical initial pressure for both phases at the interface. P_0 is the background pressure.

Eq. (10) gives the explicit relationship between the pressure and the density, which leads to an explicit algorithm developed in the multi-phase SPH model. The predictor-corrector scheme [31] and a constant time step satisfying the Courant-Friedrichs-Lewy (CFL) condition are used. According to the CFL condition, the time steps will be too small when the real sound speed of water is used. Due to this consideration, a suitable artificial sound speed is always used in weakly compressible SPH to approximate the free surface flow problems. The assumption of weakly compressible fluid satisfies that the variation of the density field,

proportional to the square of the Mach number (see Monaghan [32]), is less than 1%, i.e.,

$\Delta\rho/\rho \sim (v_{max}/c_0)^2 = Ma^2$. It should be noted that it is not the real situation [24, 26], where the

lighter phase has a larger sound speed than that of the heavier phase (i.e., $c_a > c_w$). However, in

order to prevent the pressure fluctuations, the artificial sound speed, which is 10 times of the

maximum speed of the flow field, is adopted in the simulation. Therefore, the Mach number is

smaller than 0.1.

The background pressure can be used to prevent the tension instability caused by the

negative pressure and meanwhile to keep the particle distribution uniform. However, the value

should be carefully chosen, otherwise too large background pressure can lead to some

unreasonable results, such as excessive particle resettlement, high frequency errors [33, 34].

The background pressure is added only in the model with multi-phase fluids. The term of $\chi\rho_a^2$

provides the cohesion [30] for the lighter fluid to ensure that the interface of different phases

is clear.

In order to obtain stable and accurate results, the numerical viscosity term $\mathbf{f}_v$ on the

right-hand side of Eq. (9) is included to stabilize the simulation. In the present numerical

model, the artificial viscosity by Monaghan [32] is applied:

$$\mathbf{f}_v = \alpha h \sum_j \frac{c_i + c_j}{\rho_i + \rho_j} \frac{(\mathbf{v}_i - \mathbf{v}_j) \cdot (\mathbf{r}_i - \mathbf{r}_j)}{\left|\mathbf{r}_i - \mathbf{r}_j\right|^2 + (0.01h)^2} \nabla_i W_{ij} V_j \tag{11}$$

Where, α is the artificial viscosity coefficient, h is the smoothing length, c is the

artificial sound speed. When fluid particles approach each other, the performance of the

artificial viscosity term is a repelling force and vice versa. The difference from the Colagrossi

and Landrini [24] model is that the condition of $(\mathbf{v}_i - \mathbf{v}_j) \cdot (\mathbf{r}_i - \mathbf{r}_j) < 0$ is not applied in the

calculation of the artificial viscosity term.

It is noted that, the approximation error can be caused due to the truncation of the support domain when the fluid particles are close to the boundary. In order to reduce it, a weighted average or Shepard's interpolation [35] of the density is introduced the corrected density

$$\rho_{i \in \Omega_x}^{new} = \sum_{j \in \Omega_x} \rho_j \overline{W}_{ij} V_j \tag{12}$$

Where the kernel correction is

$$\overline{W}_{ij} = \frac{W_{ij}}{\sum\limits_{j \in \Omega_x} W_{ij} V_j} \tag{13}$$

The symbols $i, j \in \Omega_x$ represent that the support domain for the continuity correction of fluid particles includes the same phase particles only. This correction is performed every 20 steps. The corrected density can also reduce the energy dissipation caused by the artificial viscosity term.

Since the flooding process of a damaged cabin is a large scale problem, the Weber number is much greater than 1.0. The role of surface tension can be ignored, so the surface tension model is not included in the present model.

The present multi-phase SPH model is carried out based on the model of [24] and stable results can be obtained. They can attribute to the following treatments: the volume-based governing equation, the density renormalization[35], the smooth interpolation at the fluid-solid interface[36], the background pressure, the cohesion force for the lighter phase and the artificial speed of sound.

2.2. Boundary pressure and floating body motion

The flooding process of a damaged cabin is a complex dynamic problem involving the hull, the inflow fluid, the outer fluid and other coupled factors. The solution of the boundary

particle is a key issue in SPH method. In this paper, the dummy particle method [36] is adopted. Three layers of particles are laid to model the cabin and the fixed boundary, which ensures that the particles from the inner and outer fluid field have no direct interaction. The pressure of the boundary particle is obtained by interpolating from the adjacent fluid particles, and the final boundary particle pressure can be expressed by Eq. (14) [36, 37].

$$P_b \approx \sum_{j\in\Omega_w} V_j W_{bj} \left[\rho_j \left(m_b/m_j \frac{D\mathbf{v}_b}{Dt} - \mathbf{g} \right) \cdot \mathbf{r}_{bj} + P_j \right] \Big/ \sum_{j\in\Omega_w} V_j W_{bj} \tag{14}$$

Where, the acceleration of the fixed wall boundary particle is

$$\frac{D\mathbf{v}_b}{Dt} = (0,0) \tag{15}$$

For boundary particles of the cabin model,

$$\frac{D\mathbf{v}_b}{Dt} = \frac{D\omega}{Dt} \times \mathbf{r}_{bG} + \omega \times \omega \times \mathbf{r}_{bG} \tag{16}$$

Where ω is the angular velocity, $\mathbf{r}_{bG}$ is the position vector of the boundary particle b pointing to the centre of the mass G.

The densities of the solid wall boundary particles and the cabin boundary particles are obtained by solving the state equation of Eq. (10),

$$\rho_b = \rho_{w0} (\frac{P_b - P_0}{B} + 1)^{1/\gamma_w} \tag{17}$$

The translation and rotation of the damaged cabin can be obtained by

$$M \frac{D\mathbf{V}}{Dt} = \sum_{b\in\Omega_b} m_b \frac{D\mathbf{v}_b}{Dt} + M\mathbf{g}$$
$$I \frac{D\omega}{Dt} = \sum_{b\in\Omega_b} m_b \mathbf{r}_{bG} \times m_b \frac{D\mathbf{v}_b}{Dt} \tag{18}$$

Where M is the mass of the damaged cabin, I is the moment of inertia, $\mathbf{V}$ is the velocity of the cabin barycentre.

9

2.3. Numerical model validation

In order to verify the accuracy and stability of the present multi-phase SPH model, the following two benchmarks are simulated, i.e., the classical dam-break and the sinking process of an intact rigid box. The results are compared with the experimental or numerical results.

2.3.1. The dam-break

The initial numerical model of the multi-phase dam-break is shown in Fig.1, in which the same dimension and arrangement are adopted as the experiment in Zhou et al. [38]. The height of the dam-break is $h_w = 0.6m$, the length of the dam-break is $l = 2.0h_w$, the solid wall boundary length is $L = 5.36h_w$ and the height is $H = 3.0h_w$. Instead of simulating the remove process of the gate, considering the pressure fluctuation caused by removing the gate, the hydrostatic pressure derived by Greco [39] and Pohle [40] is given directly in Eq. (19) and the pressure distribution is plotted as Fig.1.

$$P_w(x, z) = \rho_{w0} g(h_w - z) - \frac{8\rho_{w0} g h_w}{\pi^2} \sum_{m=0}^{1000} [\frac{1}{(2m+1)^2} e^{(2m+1)\pi x/(2h)} \cos(\frac{2m+1}{2h_w} \pi z)] \qquad (19)$$

Where $\rho_{w0} = 1000.0 kg/m^3$, the coordinate xOz is indicated in Fig.1. The pressure probe is located at the wall and $r_0 = 0.267h_w$ away from the bottom. The radius of the pressure sensor in the experiment [38] is $45mm$. The distribution of the particles in the computational model is uniform with a particle spacing $dx = dz = h_w / 120$. The artificial sound speed in water is $c_0 = 10\sqrt{gH}$, a constant time step of 1e-6s is used and the artificial viscosity coefficient is $\alpha = 0.03$. The parameters in Eq. (10) are $P_0 = 500.0Pa$ and $\chi = 0.5$ respectively. The dimensionless scale for the time is $t \sim t(g / h_w)^{0.5}$, and for the velocity is $v \sim v/(gh_w)^{0.5}$.
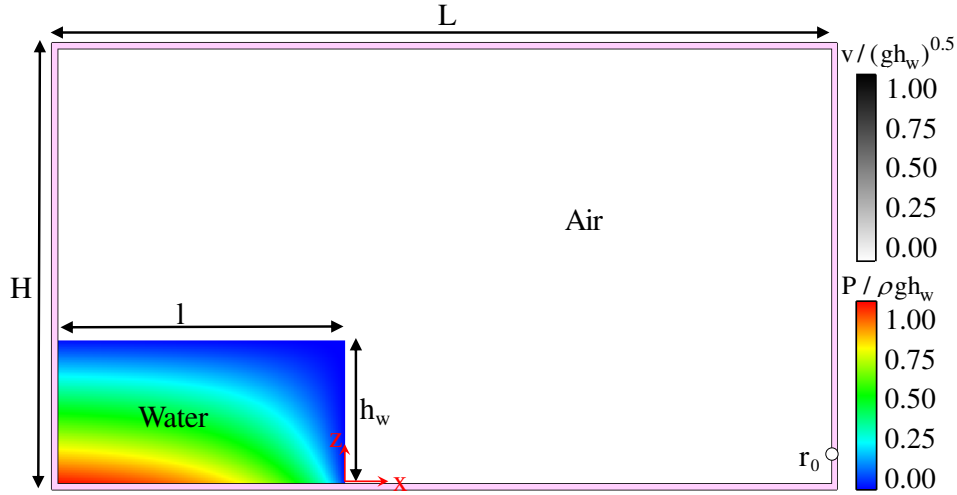
Fig. 1. The numerical model of dam-break.

The pressure distribution for water and the velocity distribution for air at several instants are shown in Fig.2. The water impacts the right wall and climbs along the wall shortly after the break and the pressure at the probe reaches the peak quickly in Fig.2 (b). Some water particles are seen carrying large velocities and splashing into air field as shown in Fig.2 (c) and (d). It is evident in Fig.2 (d) that when the water overturns, the air entrapment in the closed water chamber occurs which further induces the oscillation of the pressure in the water field. The pressure distribution of the field remains continuous in the whole flow process and the interface of the water and air can be clearly observed in Fig.2. Due to the high particles resolution ratio, the pressure field is smoothed without any post-processing method.

The comparison of the pressure on the probe between numerical results and experimental data (Greco [39]) is shown in Fig.3. The results of numerical simulations are in good agreement with the experimental data. The pressure oscillation is seen occurring at the closing time of the water tongue. Compared to the numerical results without considering air in the cabin, the pressure on the probe obtained from the multi-phase model considering air effect is clearly

more consistent with the experimental measurements. The local amplification of the water tongue corresponding to the moment of the pressure peak is also clearly observed in Fig.3. The multi-phase SPH method developed in this paper presents stable and accurate results for the dynamic process of the dam-break case.
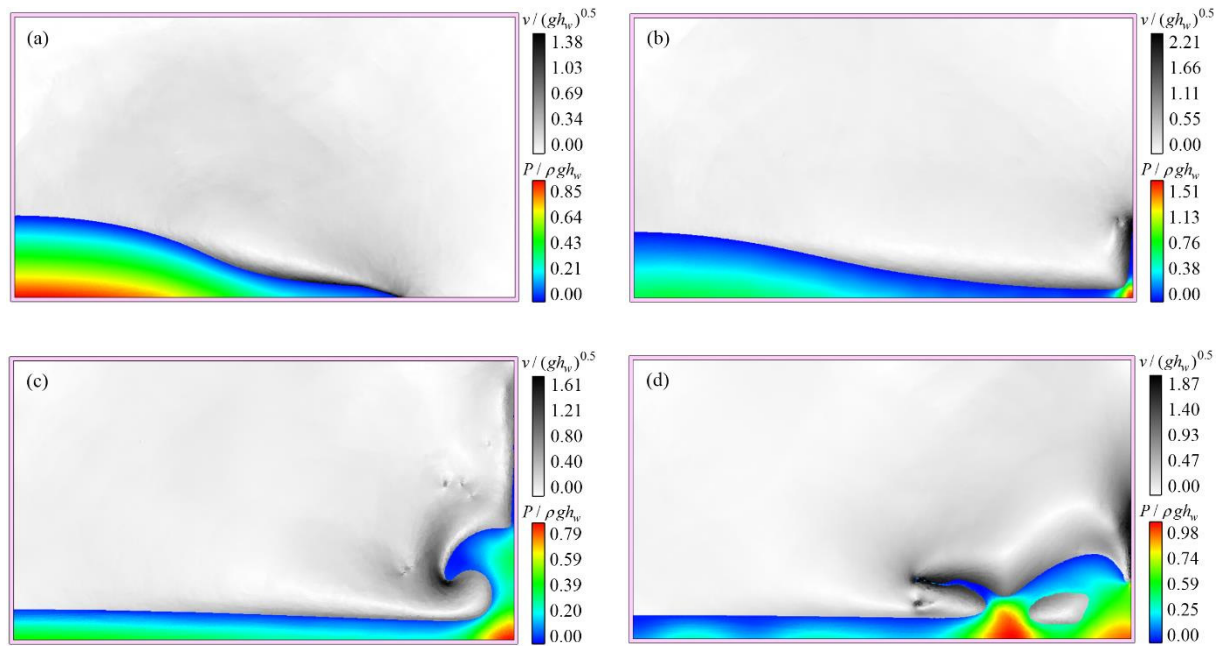

Fig. 2. The multi-phase dam-break process, pressure distribution for water and velocity distribution for air. (a) $t = 1.74$, (b) $t = 2.75$, (c) $t = 5.87$, (d) $t = 6.75$.
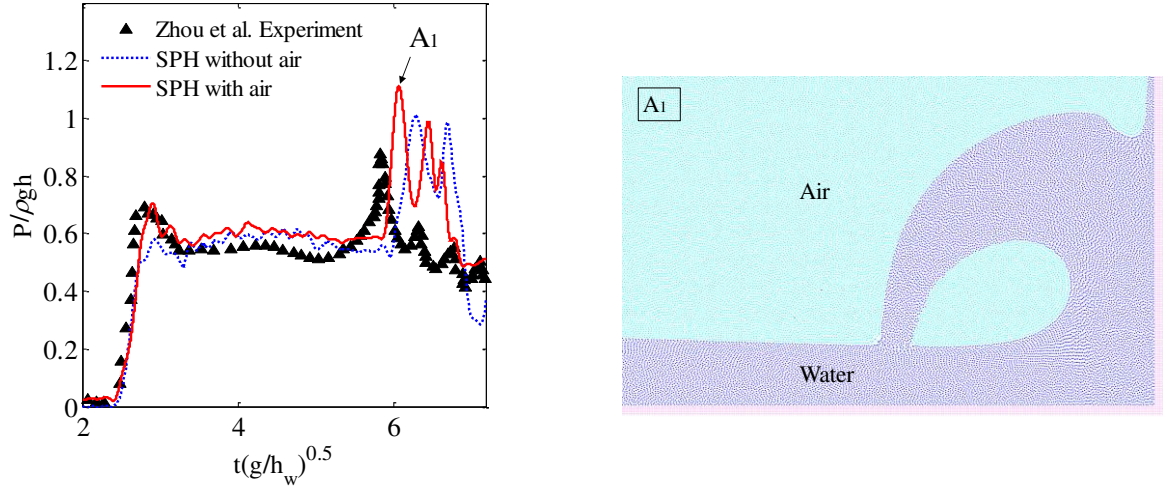
Fig. 3. The dam-break solutions from SPH and the experiment. Left: Comparison between numerical and experimental [38] results. Right: the particle distribution corresponding to the moment of the pressure peak.

In order to study the energy conservation of the multi-phase model, the evolution of the mechanical energy of the dam-break case is presented in Fig.4. The total energy variation is calculated by the equation

$$\varepsilon = (E_{kt} + E_{pt} + \Delta e - E_{pt}^0) / E_{pt}^0 \tag{20}$$

Where E_{kt} and E_{pt} are the total kinetic and potential energy of the fluids respectively, the superscript '0' represents the initial time, and Δe is the change of the internal energy[20]. It can be observed in the Fig.4 that the impacts between the fluid and the wall or between the fluid and the fluid cause the energy loss. In the multi-phase model, the energy loss with air flow is faster than the model without air. The use of Shepard interpolation with the interval $n = 20$ produces a better conservation of the total energy.
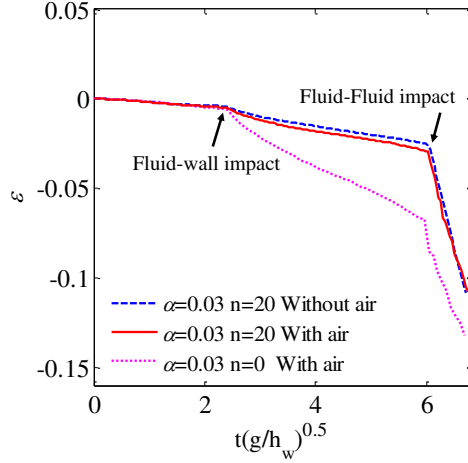
Fig. 4. The total energy evolution of the dam-break solutions.

2.3.2. The sinking process of an intact box

To further validate the present multi-phase SPH model, the sinking process of an intact rectangular box with an asymmetric mass in the viscous fluid is simulated. The configuration of the sinking object is the same as that in Barcarolo [41]. As shown in Fig.5, the length of the rectangular box is $l = 1.0\text{m}$, the height is $0.5l$, and the centre of gravity is $G = (0.75\text{m}, 0.0\text{m})$. The effect of the lighter fluid on the sinking process is studied. The density ratio between the heavier and the lighter fluid is $\rho_H / \rho_L = 1000$. The acceleration of the gravity is $\mathbf{g} = (0, -1.0)\,\text{m/s}^2$. The weight of the box is $m = 1.0\text{kg}$ and the inertia moment is $I = 0.083\text{kg}\cdot\text{m}^2$. The kinematic viscous coefficient of the heavier fluid is $\upsilon = 0.002\text{m}^2/\text{s}$, as used in Barcarolo [41]. The relationship between the artifical viscosity parameter α in Eq. (11) and the kinematic viscosity υ given by Monaghan [32] is:

$$\alpha = 8\upsilon(hc_0)^{-1} \tag{21}$$

The computational domain has a width of $4l$ and a height of $5l$. The height of the heavier phase is $3l$. The artificial sound speed of the heavier phase is $c_0 = 10\sqrt{3gl}$ and a

constant time step of $dt = 5e-6s$ is used. The parameters in Eq. (10) are $P_0 = 1.0\text{Pa}$ and $\chi = 0.2$. The dimensionless time is scaled by $t \sim t(g/3l)^{0.5}$. Uniform particle distribution is assumed in the whole simulation field with three particle spacings $dx = dz = 1/25$, $dx = dz = 1/50$ and $dx = dz = 1/100$.
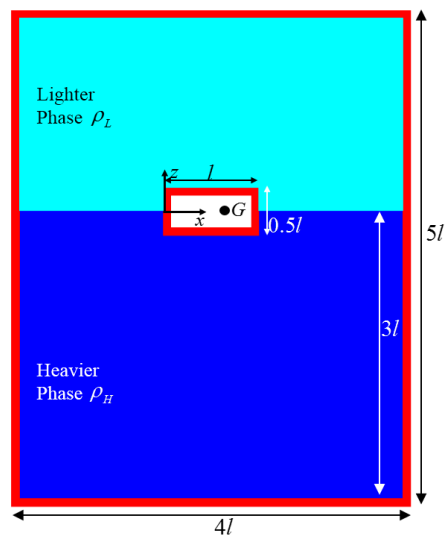

Fig. 5. The sinking model of an intact box.

The vertical displacement and the rotation angle of the rectangular box during the sinking process are shown in Fig.6 respectively. The multi-phase SPH results are compared with those from the finite volume particle method (FVPM) and the Riemann-SPH method with particle resolution $dx = 1/100$ [41]. Due to the asymmetric mass distribution, the sinking process is accompanied by rotational motions under the moment of gravity and buoyancy. It is evident that the trends of the present SPH results are in good agreements with those of FVPM and Riemann-SPH results, which demonstrates that the multi-phase SPH model is robust in solving such fluid-solid interaction problems. In addition, good convergence of the SPH model is also shown in the figure.
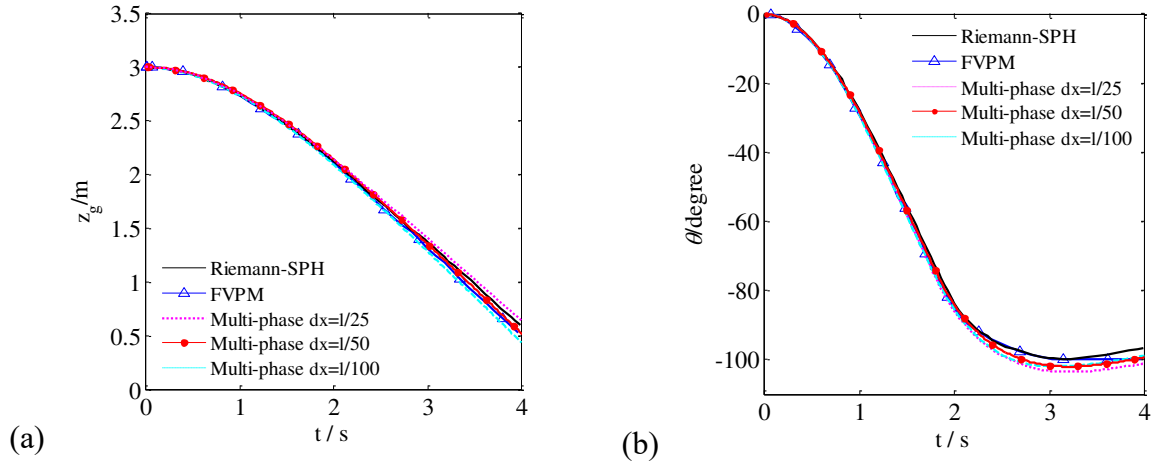
Fig. 6. Motions of the intact box compared with the simulation results in Barcarolo [41].

(a) Vertical displacement of the barycentre, (b) Heeling angles of the intact box.

To reveal the fluid physics by the present multi-phase SPH model, the comparision between the results of particle resolution $dx = dz = 1/100$ with and without the lighter phase at the same time instantaneouses is shown in Fig.7. The first cavity is formed when the free surface flips and involves the lighter phase fluid at the right hand side of the box, as shown in Fig.7 (a). With the sinking continuing, the box approaches to fully submerging in the heavier fluid, see in Fig.7 (b), the second cavity is formed as the water closing at the top of the box. The first cavity is seen moving with the box in the multi-phase flow model. The evolution of the free surface is captured in detail by the present multi-phase SPH model. When the free surface is completely closed, two jets are formed up and down in the multi-phase flow results, as shown in Fig.7 (c). The two cavities are gradually integrated when the box continues to sink. In Fig.7 (d), due to the closure and collision of the free surface, the water mound is formed. For the model without the lighter fluid, the surrounding of the box is filled with the heavier liquid. However, for the multi-phase model, the box is partially surrounded by the lighter fluid

16

in the sinking process, and a long trail is formed behind the box.

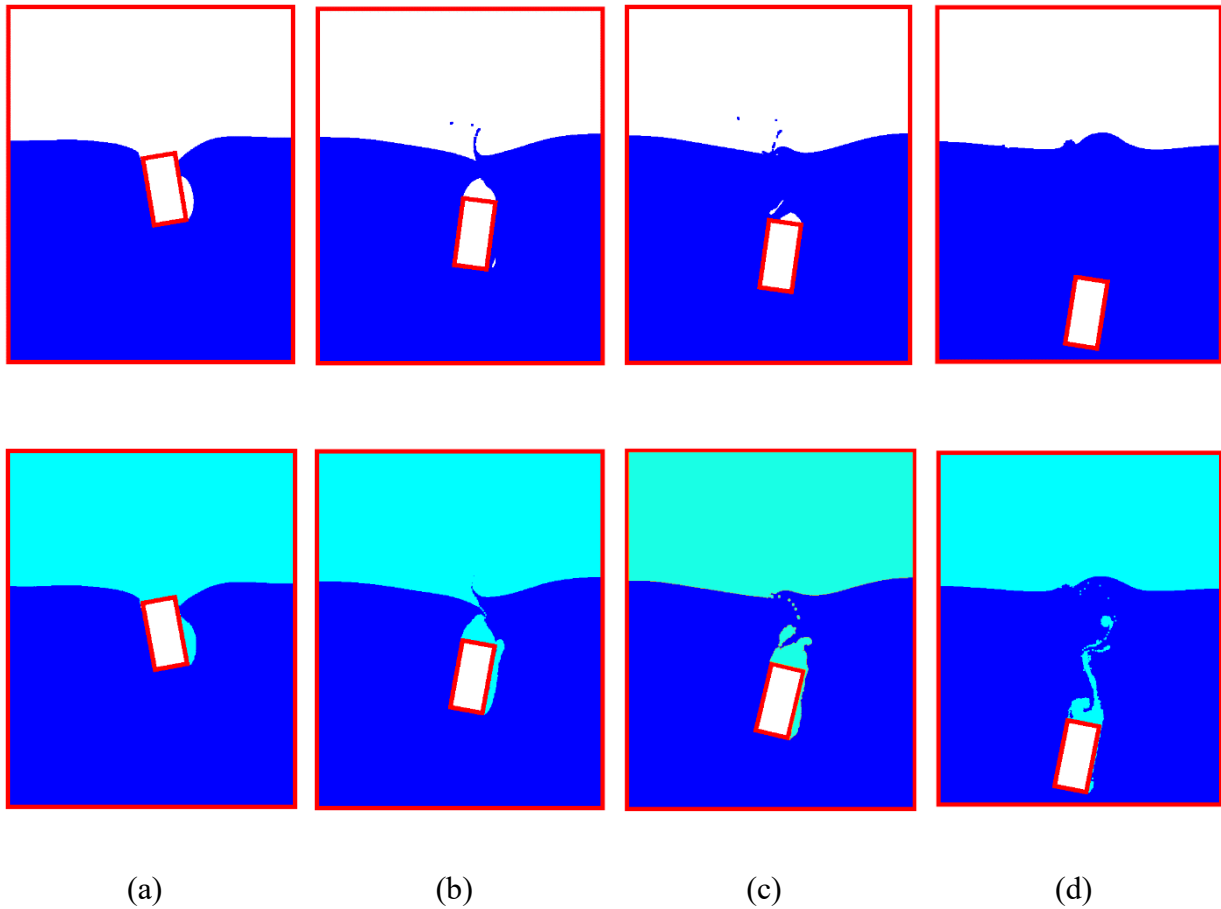(a)   (b)   (c)   (d)

Fig. 7. The comparison of the sinking process. Up: without the lighter phase, Down: with the lighter phase. (a) $t = 1.03$, (b) $t = 1.44$, (c) $t = 1.55$, (d) $t = 2.21$.

The motion trajectories of the sinking process predicted by the two models are shown in Fig.8. The effect of the lighter fluid on the box motion is not obvious before the the formation of the cavity. When the free surface is closed, the lighter fluid start to interact with both the heavier phase fluid and the boundary of the box which will affect the resultant force. The difference shows the lighter fluid has obvious effects on the horizontal displacement in the sinking process, as shown in Fig.8. The sinking and rotation velocities of the rectangular box

obtained by the multi-phase model are smaller than those from the single-phase model after the lighter fluid involved into the free surface formation of the heavier fluid.
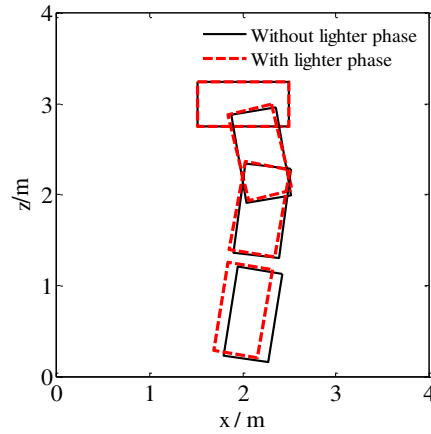

Fig. 8. The trajectory of the sinking box.

3. Results and discussions

3.1. Description of case matrix

Most cabins in seagoing vessels or offshore service vessels are not watertight, and they normally have openings on the bulkhead, deck opening, man-hole and air pipe. Since the air can escape from the openings, therefore, it is necessary that the air is properly considered in simulating the flooding process. Two types of openings are considered in this study: the opening at the waterline and that on the upper bulkhead.

The cabin model has a cross section of U-shape with a breadth of $B = 16.0m$, a depth of $D = 8.5m$, a draught of $d = 4.2m$. The position of the centre of gravity is $G = (35.0, 0.2)$, as shown in Fig.9. The height of the opening on the broadside is $b = 4.0m$ and the centre of the opening is located at the free surface. The depth of the water in the simulation domain is $h_w = 20.0m$. The uniform particle distribution is adopted here and the particle spacing is

$dx = dz = h_w / 200$. The background pressure is $P_0 = 1000.0 \text{Pa}$ and the cohesion parameter is $\chi = 0.5$. A constant time step of $1 \times 10^{-5}\text{s}$ is used in the case considering air. The parallel code with OpenMP language takes about 32 minutes for 10 thousand steps when running on a computer equipped with Intel i7-6700 (4 cores, 4.0 GHz). For different cases, the total numbers of particles are different with approximately 260 thousand of particles for the multi-phase flow model. In order to study the effect of the air flow on the flooding process, seven cases are included in the present numerical simulation: (1) the damaged cabin without air; (2) the damaged cabin without deck opening; (3) the damaged cabin with an opening at the centre of the upper deck and the width of the opening $\delta = 1/2b$; (4) the width of the opening at the centre of the upper deck is $\delta = 1/4b$; (5) the width of the opening at the centre of the upper deck is $\delta = 1/8b$; (6) the width of the opening at the centre of the upper deck is $\delta = 1/10b$; (7) three openings $3\delta = 1/4b$ on the upper deck and the distance between the openings is about $B/3$. The air is considered in the latter six cases except case (1) (see Table 1).
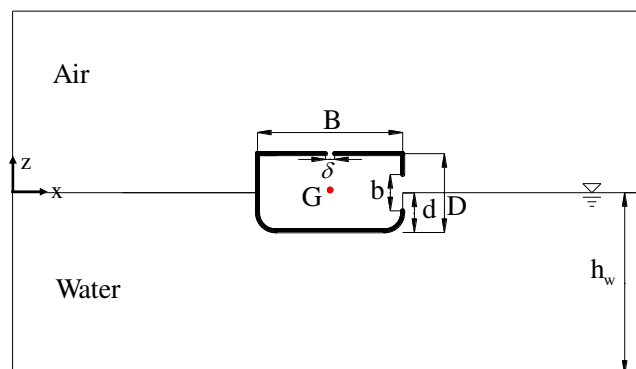

Fig. 9. The numerical model.

Table 1 Simulation cases.

No.	Opening on deck	Air flow
Case 1	None	No
Case 2	None	Yes
Case 3	$\delta = 1/2b$	Yes
Case 4	$\delta = 1/4b$	Yes
Case 5	$\delta = 1/8b$	Yes
Case 6	$\delta = 1/10b$	Yes
Case 7	$3\delta = 1/4b$	Yes

3.2. The air capture in the flooding process

When the air is unable to escape timely in the flooding process, an air cushion will be formed in the cabin. The air in the cabin will therefore interact with the inflow water and the hull, thus the flooding process may be altered.
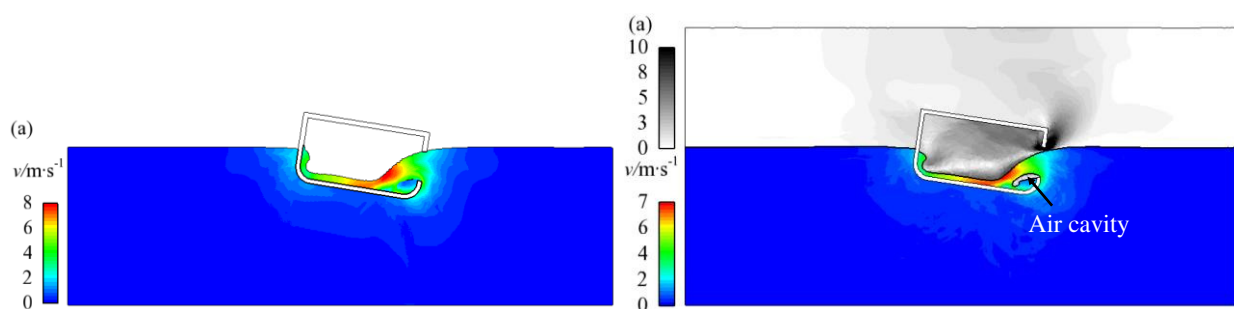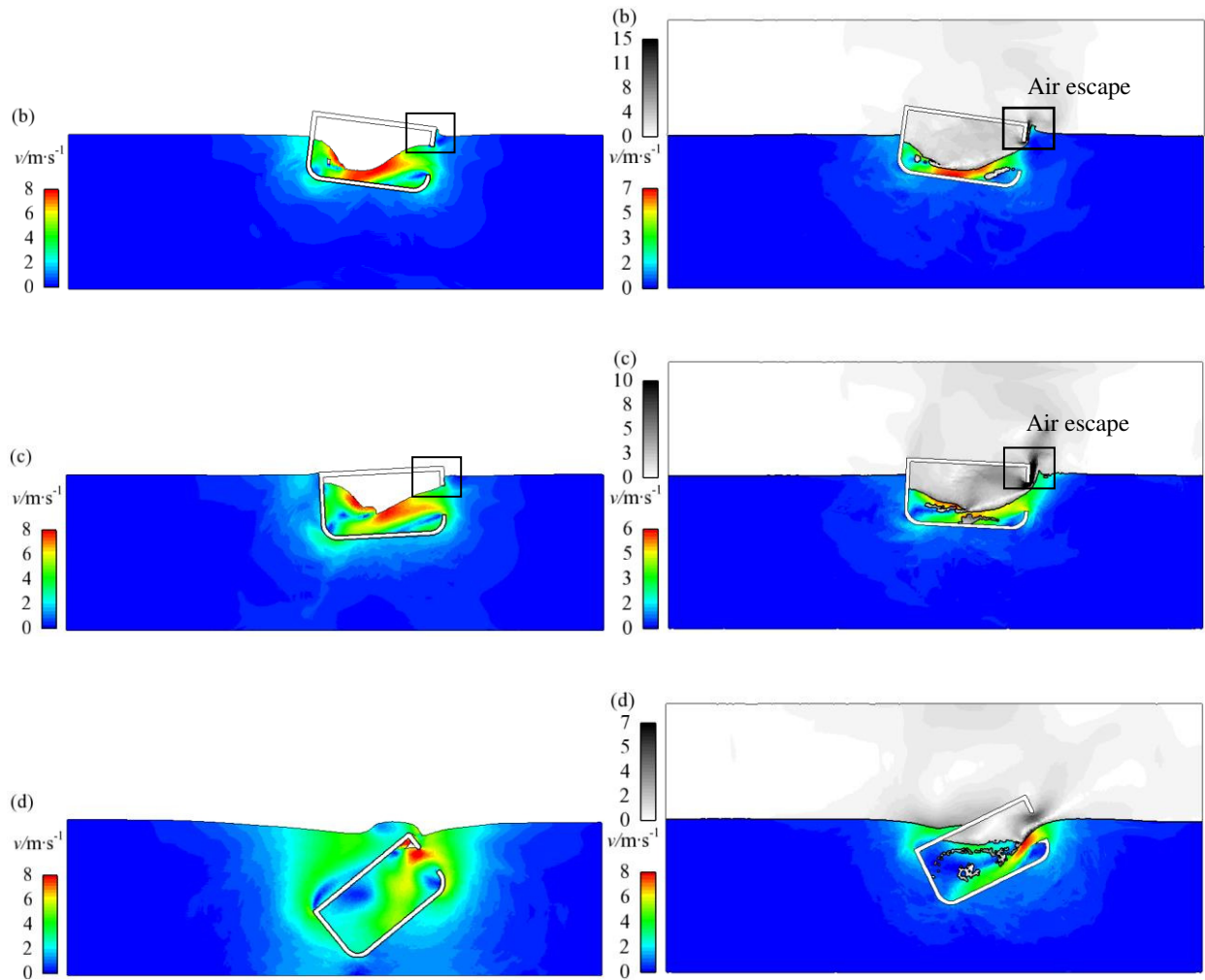
Fig. 10. Comparison of the damaged cabin motion without air (left) and with air (right), (a) $t = 4.0s$; (b) $t = 5.0s$; (c) $t = 6.0s$; (d) $t = 10.0s$.

The flooding processes of the watertight damaged cabin with air flow and without air flow effect are illustrated in Fig.10, where the flow field is colored by the velocity. The external water begins to flow into the cabin once the cabin is released with some air being entrapped forming an air cavity near the opening. As shown in Fig.10 (a), the flooding water moves quickly and turns over at the wall opposite broadside of the opening; the air is seen escaping from the opening initially but soon the damaged cabin is heeled towards the opening side

(Fig.10 (b)). With the continuous flooding, accompanying to the heeling alternate side of the cabin, the air continuously escapes from the opening while substantial air cavity is seen entrapped in the water inside cabin (Fig.10 (c)). Finally, as the cabin further submerges with the opening under the water surface, the entrapped water cavity is seen spreading into smaller cavities inside cabin while the exhaust is terminated (Fig.10 (d)). In contrast to the case without considering air, a clear phase delay in submersion of the damaged cabin due to the dynamic exchange of air and water (between air and in flow water at the opening as well as between the air cavities and flooding water inside cabin) is clearly observed during the flooding process for the damaged cabin motion with air considered.
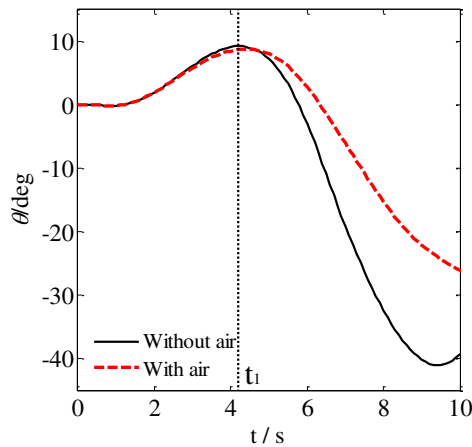

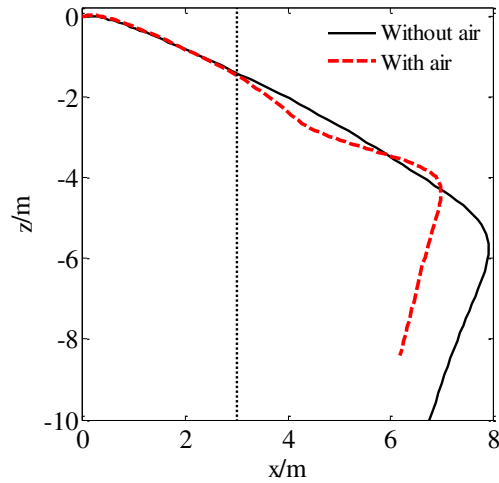Fig. 11. Comparison of the heeling angle with air and without air.

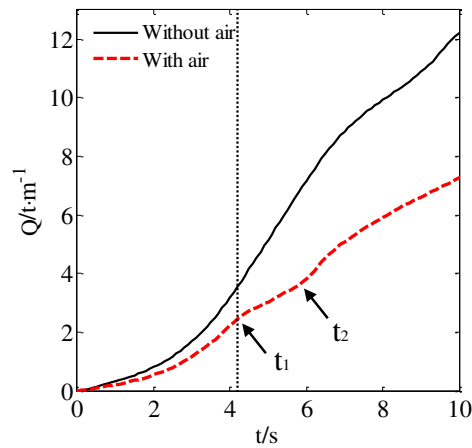Fig. 12. The effect of air on the displacement of the barycentre.

Fig. 13. The effect of air on the amount of flooding water.

The heeling angle, the displacement of the barycentre and the amount of flooding water when considering air and without air are presented in Fig.11, Fig.12 and Fig.13 respectively. As can be seen in Fig.11 and Fig.12, the effect of air is not obvious before the damaged cabin reaches the initially maximum heeling angle to the opening broadside, especially for the displacements of the barycentre, it is almost identical to the case without air. However, beyond

that, the air effect is also seen, it reduces the heeling angle significantly. Since the air can only escape from the opening of the cabin, the influence on the amount of flooding water is obvious even at early stage of the process, as shown in Fig.13. Due to the air escaping from the opening of the damaged cabin, the amount of inflow water is approximately half of that for the case without considering air at the same time instantaneous. The significant change of flooding rate occurs at two time instants t_1 and t_2 in Fig.13: the first one occurs when the cabin reaches the initially maximum heeling angle while the top of the opening submerges below the water surface; the other one is when the damaged cabin heels to the opposite side, the damaged opening beginning to rise. Due to the dynamic exchange process of the air and water at the opening, the amount of flooding water is significantly decreased.
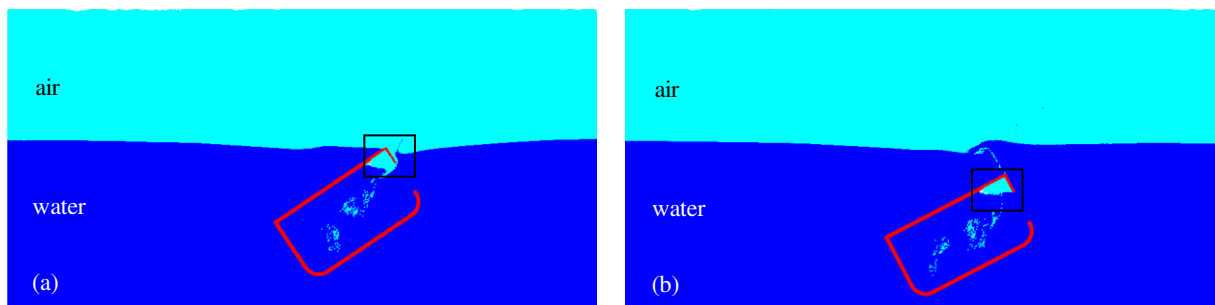

Fig. 14. Formation of the air pocket in the sinking process. (a) $t = 13.20s$, (b) $t = 14.40s$.

The formation of the "air pocket" during the sinking process of the damaged cabin is shown in Fig.14. Due to continuous flooding, the damaged cabin is seen submerged further with the opening being fully blocked by water, the remaining air in the damaged cabin is unable to escape and trapped to form the "air pocket". Such air pocket plays an important role in the maritime rescue and impacting the stability of a damaged ship.

3.3. The air flow for different opening sizes

For operation purpose, deck and/or bulkheads are often fitted with openings. The air can escape from them when they are open and the flow field characteristics in the damaged cabin is affected during flooding process. The velocity distribution of the flow field (for both air and water) for the four cases (case3-case6) at two time instants are shown in Fig.15. The figures at the same time are colored with a same legend. Under the moment formed by the flooding water, the cabin heels to the opening broadside with the top of the opening below the waterline, as shown in Fig.15 (1) at $t = 5.1s$. The broadside opening is fully closed by the flooding water at these cases but the air can escape from the deck opening. The air velocity at the centre of the deck opening reaches the maximum and the air field carries a large kinematic energy at this moment. There is a low air velocity area near the free surface of the inflow water, which is caused by the formation of the air vortex. The air near the free surface will follow the flooding water motion and the extra air is pushed by the flooding water to move to the openings, thus the air vortex is formed. Such air vortex formed in the damaged cabin increases the energy loss of the flow filed. The larger the deck opening, the faster the diffusion of the air vortex. Also, the air resistance caused by the air vortex decreases. With the increase of the deck opening size, the air escaping velocity decreases while the maximum flow velocity of the flooding water in the cabin increases. As the flooding process continues, the flooding water from the broadside pushes the inflow water to the opposite side which causes the cabin to reversely heel, as shown in Fig.15 (2) at $t = 7.2s$. At this moment, the air is seen to escape from both the broadside opening and the smaller deck opening. With the increase of the deck opening size, the velocity of the flooding water increases and the kinematic energy of the inflow water also increases. Therefore, the height of the inflow water climbing along the wall and the accumulation of the water at the opposite broadside of the opening increases. The energy of the inflow water

25

reduces as a direct consequence of the energy exchange between the air and water.
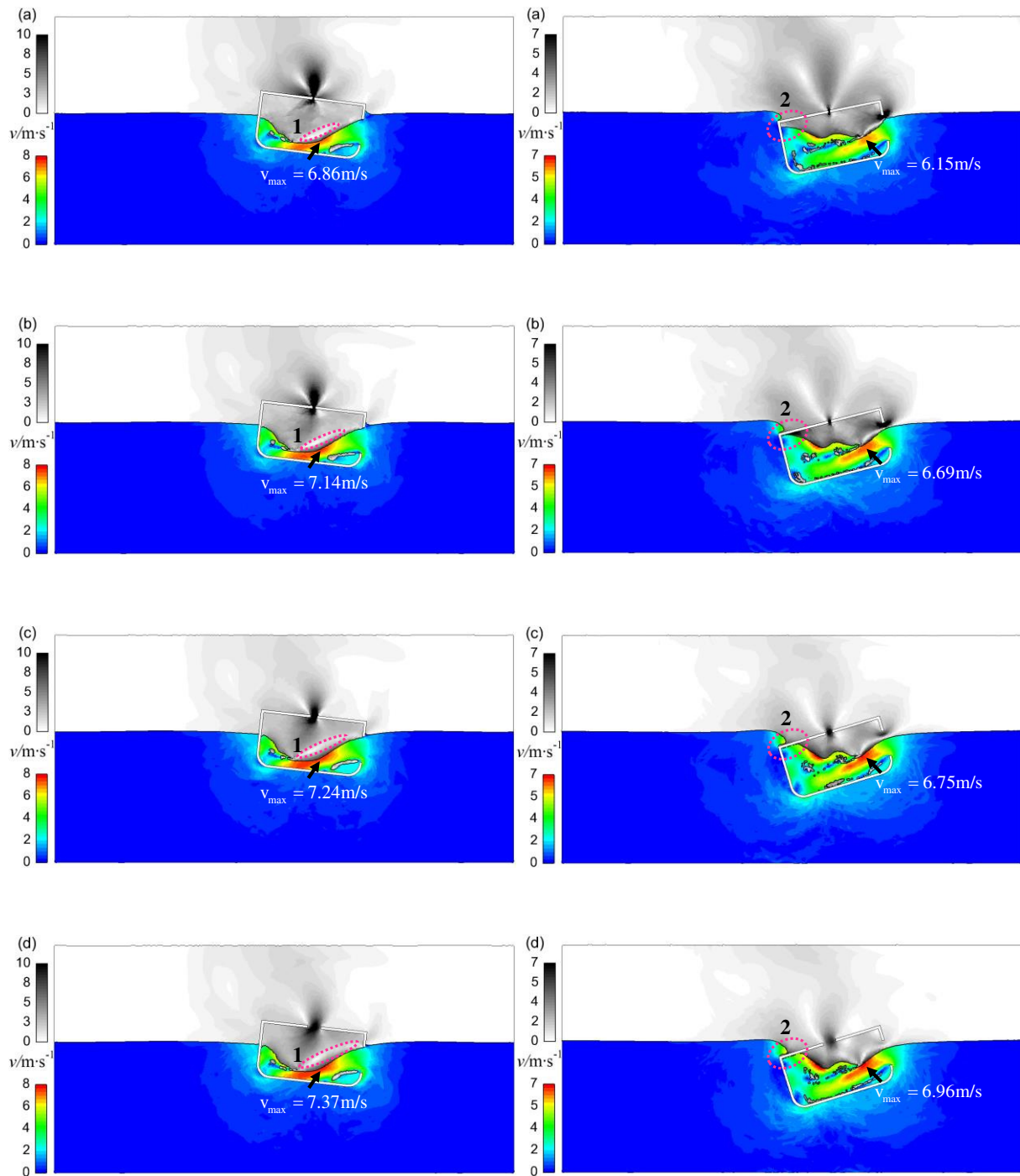
(1) t = 5.1s   (2) t = 7.2s

Fig. 15. The velocity of the flow field during the flooding process of the cabin with deck opening. (a) $\delta = 1/10b$; (b) $\delta = 1/8b$; (c) $\delta = 1/4b$; (d) $\delta = 1/2b$. The circle 1 marks the zone with a low air velocity and the circle 2 marks the water height accumulated in the broadside.

The velocity of the flow field at the centre of the deck opening is shown in Fig.16, the positive value represents the outflow and inversely the negative value represents the inflow. With the increase of the deck opening size, the velocity of the flow field at the centre decreases. When the deck opening is greater than $\delta > 1/8b$, the peak velocity is in inverse proportion to the opeing size.
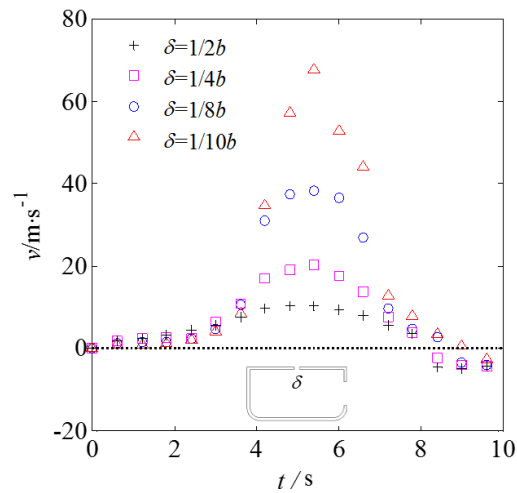
Fig. 16. The flow velocity at the centre of the deck opening with different sizes.

Heeling angles for different deck opening sizes are shown in Fig. 17. With the decreasing of the deck opening size, the positive maximum heeling angle increases while the negative maximum heeling angle decreases. The amount of flooding water is almost consistent for the

four cases with different deck opening sizes (see Fig.18). For the damaged cabin with deck opening of different sizes, the influence of air flow before the cabin reaching the positive maximum heeling angle is not obvious, so the moment caused by the accumulated water is the main factor for the heeling motion at this stage.
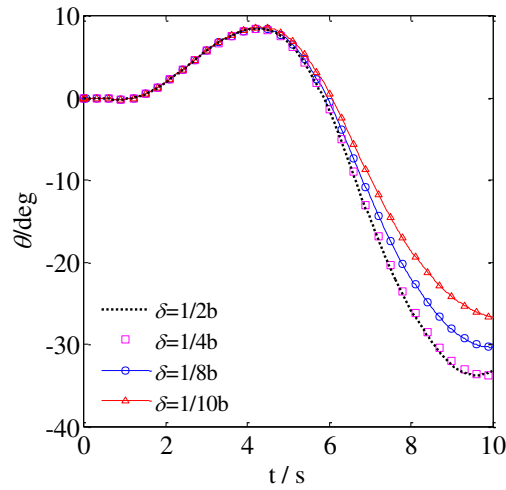

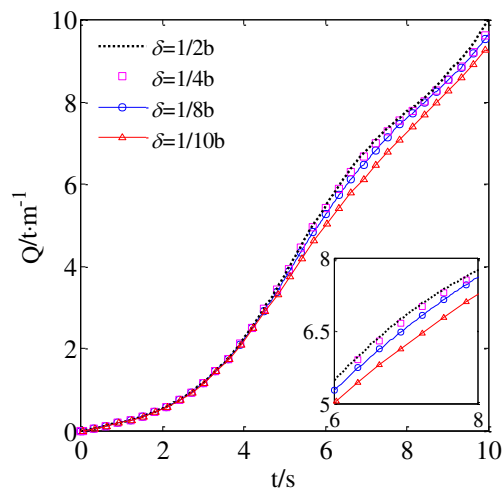Fig. 17. The effect of the deck opening sizes on the heeling angle.

Fig. 18. The effect of deck opening sizes on the amount of flooding water.

Fig.19 shows the velocity of the barycentre in the flooding process of the cabin with

different deck opening sizes. There are two inflection points clearly visible in the curves of the horizontal velocity in Fig.19 (a) and the vertical velocity in Fig.19 (b). The first inflection point appears at the moment of the cabin reaching the maximum heeling angle to the opening side and the second one is caused by the green water on the deck of the opposite side. Affected by the amount of the flooding water and the air cushion in the cabin, the horizontal drifting velocity and the sinking velocity are both reduced with the decreasing of the deck opening size. It can be clearly observed that the increase of the deck opening size has less effects on the flooding process of the cabin when the deck opening is greater than $\delta > 1/4b$.
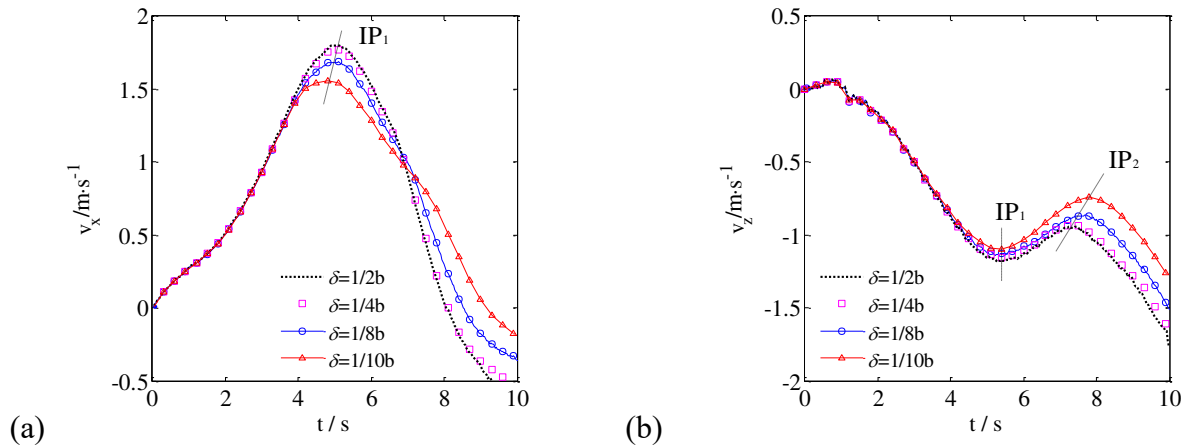

(a)   (b)

Fig. 19. The effect of the deck opening sizes on the velocity of the barycentre. (a) The horizontal velocity of the barycentre, (b) The vertical velocity of the barycentre.

3.4. The air flow for different opening numbers

Taking the deck opening size $\delta = 1/4b$ for example, the numbers of openings are increased to three with $3\delta = 1/4b$ for each opening. The openings are equally distributed on the upper deck.
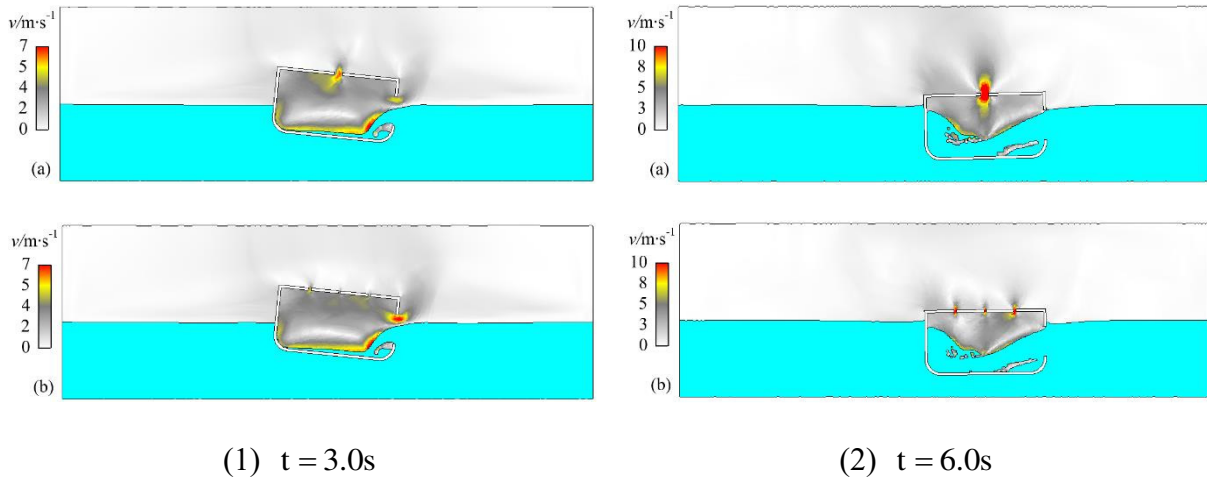
(1) t = 3.0s   (2) t = 6.0s

Fig. 20. The velocity of the air field for the damaged model with different deck opening numbers, (a) deck opening $\delta = 1/4b$; (b) deck opening $3\delta = 1/4b$.

The velocity distribution of the air field for the damaged model with different opening numbers at two time instants are shown in Fig.20. For the case of $3\delta = 1/4b$, the velocity of the air flowing out from the damaged opening is larger than the case of one opening on the deck, as shown in Fig.20 (1) at t = 3.0s. In Fig.20 (2), at t = 6.0s, for the case of $3\delta = 1/4b$, there is a low velocity zone occurring at the opposite of the broadside opening. The outflow velocity of the air at the deck opening near the damaged broadside is larger than that of the other two openings. Although the total opening size is same, the opening numbers alter the air flows. Generally, the velocity of the air flow in the cabin decreases when increasing the opening number.

The centre velocity at the middle deck opening is shown in Fig.21. The positive value represents the outflow and inversely the negative value represents the inflow. Obviously, the centre velocity of the model $3\delta = 1/4b$ is smaller than the one deck opening case. It may be attributes to that the deck opening distribution affects the air flow direction and further the velocity magnitude.
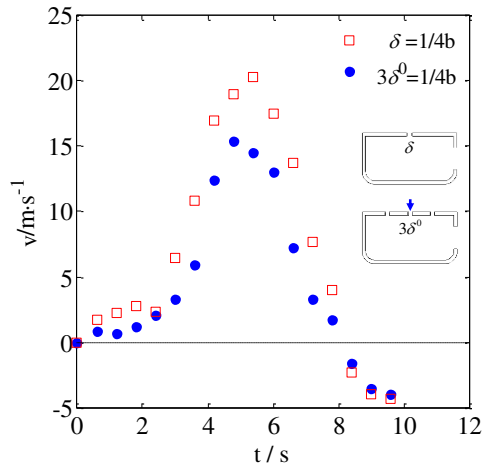
Fig. 21. The comparison of the centre velocity of air on the upper deck opening for the models with different opening numbers.

In Fig.22, (a) heeling angle of the models, (b) the trajectory of the barycentre and (c) the position of the cross section are shown respectively. The difference of the model motion occurs when the damaged opening is fully submerged. The trends of the motion for the two models is similar, but the magnitudes of the heeling angle and the velocity is slightly smaller for the case of three deck openings. The air cushion reduces the sinking speed of the damaged cabin as shown in Fig.22 (b).
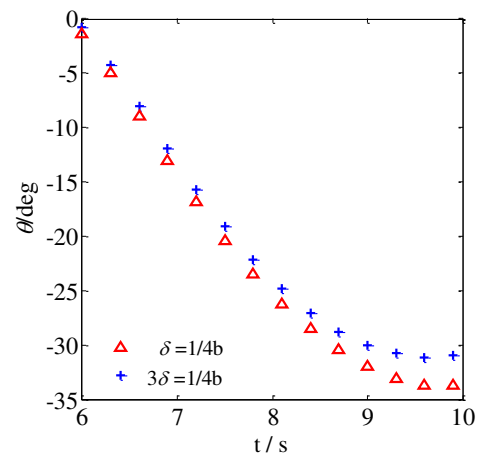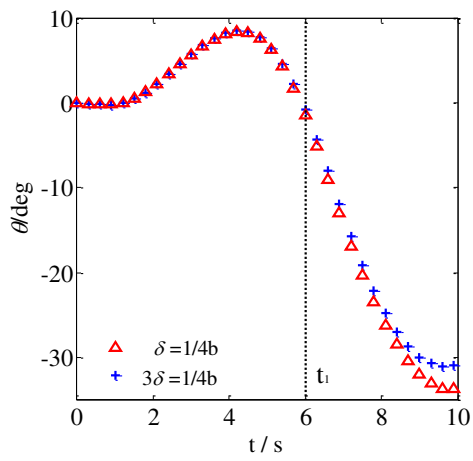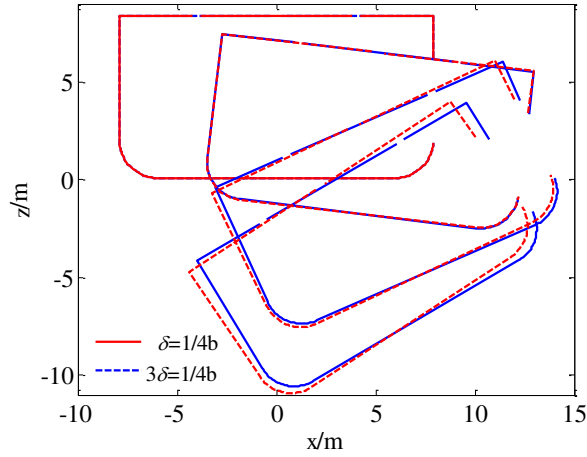
(a) The heeling angle of the models
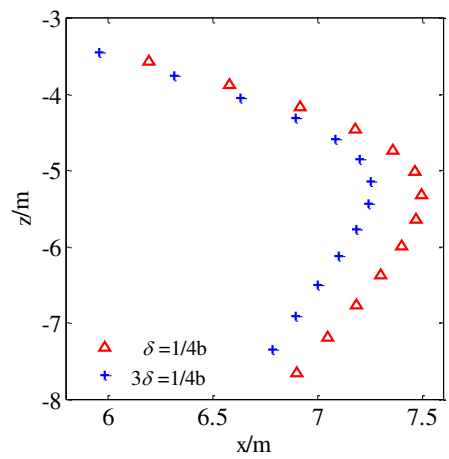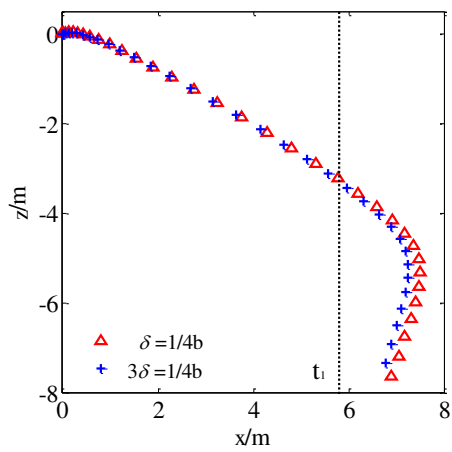
(b) The trajectory of the barycentre

(c) the position of the cross section

Fig. 22. The motion for the model with different opening numbers. The right is amplification after t_1.

The results for the damaged cabin models simulated in this paper are based on the two-dimensional model. It should be pointed out that, by considering the three-dimensional effect, the inflooding water moving along the longitudinal direction may reduce the moment by the floodwater. The effect of the buoyant force in 2D model may result in the sinking rate and the inflooding rate much higher than those in 3D models. By extending the 2D numerical model developed in this paper to 3D, the dynamic flooding process of a damaged cabin can be investigated in more realistic situation and provide direct guidance to marine operation and ship design.

4. Conclusion

In this paper, a multi-phase SPH model has been developed. Rigorous validations including the dam-break and the sinking process of an intact rectangle box, have been conducted to demonstrate the stability and accuracy of the present numerical model.

The dynamic flooding process of the damaged cabin considering the air flow is studied, and the effects of the size and number of the openings are examined. Before reaching the maximum heeling angle to the opening broadside, the motion of the damaged cabin is mainly affected by the flooding water rather than the air flow. With the flooding continuing, the dynamic exchange of air and water takes effects on the flow of the flooding water and further the force and motion of the damaged cabin.

For the damaged cabin model with openings on the upper deck, the air tends to escape from the deck opening with a high speed. When the deck opening size is $\delta = 1/10b$, the maximum air velocity at the centre of the deck opening reaches more than 10 times of the velocity of the inflow at the damaged opening. With the increase of the size of the deck opening, the effect of air flow restraining the inflow motion is weakened, but the heeling and sinking rate are increased due to the increasing amount of the flooding water. For the size of the deck opening $\delta > 1/4b$, there is less influence on the motion of the cabin, while for $\delta < 1/10b$, the amplitude of the heeling angle is approximately the same as that of the cabin without deck opening but considering air flow.

For the same deck-opening size (in total) but separating to multiple openings, the air flow in the cabin becomes complicated. When the number is increased, the air flow velocity in the cabin is generally decreased. The sinking and heeling rate is also decreased due to the effect of air cushion. It should be noted that the air is considered as a weakly compressible fluid in this study. In fact, the compressed air in airtight compartments may benefit the buoyancy of the ship but adversely it may also bring about some instabilities when it is released or unloaded. Further researches will be dedicated to extending the multiphase method to a complex compartment model and studying the air cushion formed in the cabin.

Acknowledgements

References

[1] Khaddaj-Mallat C, Alessandrini B, Rousset J-M, Ferrant P. An experimental study on the flooding of a damaged passenger ship. Ships Offshore Struc. 2012;7:55-71.
[2] Cheng H, Zhang AM, Ming FR. Study on coupled dynamics of ship and flooding water based on experimental and SPH methods. Phys Fluids. 2017;29:107101.
[3] Manderbacka T, Mikkola T, Ruponen P, Matusiak J. Transient response of a ship to an abrupt flooding accounting for the momentum flux. J Fluid Struc. 2015;57:108-26.
[4] Spyrou K, Thompson J. The nonlinear dynamics of ship motions: a field overview and some recent developments. Philosophical Transactions of the Royal Society of London A: Mathematical, Physical and Engineering Sciences. 2000;358:1735-60.
[5] Palazzi L, De Kat J. Model experiments and simulations of a damaged ship with air flow taken into account. Mar Technol. 2004;41:38-44.
[6] Hearn G, Lafforgue D, Perdriset E, Saydan D. The hydrodynamic and dynamic motion analysis of a damaged ship. The Transactions of the Royal Institution of Naval Architects Part A: International Journal of Maritime Engineering. 2008;150:1-24.
[7] Smith TWP. Wave loading on damaged ships [Ph.D. Thesis]. London, UK: University of London; 2010.
[8] Ruponen P. Pressure-correction method for simulation of progressive flooding and internal air flows. Ship Technol Res. 2006;53:63-73.
[9] Ruponen P, Kurvinen P, Saisto I, Harras J. Experimental and numerical study on progressive flooding in full-scale. Trans RINA. 2010;152:197-207.
[10] Ruponen P, Kurvinen P, Saisto I, Harras J. Air compression in a flooded tank of a damaged ship. Ocean Eng. 2013;57:64-71.
[11] Strasser C, Jasionowski A, Vassalos D. Calculation of the time-to-flood of a box-shaped barge by using CFD. Proc 10th Int'l Conf Stability of Ships & Ocean Vehicles, St Petersburg, Russia2009. p. 733-40.
[12] Bouscasse B, Colagrossi A, Souto-Iglesias A, Cercos-Pita J. Mechanical energy dissipation induced by sloshing and wave breaking in a fully coupled angular motion system. I. Theoretical formulation and numerical investigation. Physics of Fluids. 2014;26:033103.
[13] Bouscasse B, Colagrossi A, Souto-Iglesias A, Cercos-Pita J. Mechanical energy dissipation induced by sloshing and wave breaking in a fully coupled angular motion system. II. Experimental investigation. Phys Fluids. 2014;26:033104.
[14] Sun PN, Ming FR, Zhang AM. Numerical simulation of interactions between free surface and rigid body using a robust SPH method. Ocean Eng. 2015;98:32-49.
[15] Bouscasse B, Colagrossi A, Marrone S, Souto-Iglesias A. SPH modelling of viscous flow past a circular cylinder interacting with a free surface. Comput Fluids. 2017;146:190-212.
[16] Zhang AM, Cao XY, Ming FR, Zhang ZF. Investigation on a damaged ship model sinking into water based on three dimensional SPH method. Appl Ocean Res. 2013;42:24-31.
[17] Ming FR, Zhang AM, Xue YZ, Wang SP. Damage characteristics of ship structures subjected to shockwaves of underwater contact explosions. Ocean Eng. 2016;117:359-82.
[18] Zhang Z, Wang L, Silberschmidt VV. Damage response of steel plate to underwater explosion: Effect of shaped charge liner. Int J Impact Eng. 2017;103:38-49.
[19] Shadloo MS, Oger G, Le Touzé D. Smoothed particle hydrodynamics method for fluid flows, towards

industrial applications: Motivations, current state, and challenges. Comput Fluids. 2016;136:11-34.

[20] Zhang AM, Sun PN, Ming FR, Colagrossi A. Smoothed particle hydrodynamics and its applications in fluid-structure interactions. J Hydrodyn, Ser B. 2017;29:187-216.

[21] Marrone S, Colagrossi A, Di Mascio A, Le Touzé D. Analysis of free-surface flows through energy considerations: Single-phase versus two-phase modeling. Phys Rev E. 2016;93:053113.

[22] Ming FR, Sun PN, Zhang AM. Numerical investigation of rising bubbles bursting at a free surface through a multiphase SPH model. Meccanica. 2017:1-20.

[23] Hu X, Adams NA. An incompressible multi-phase SPH method. J Comput Phys. 2007;227:264-78.

[24] Colagrossi A, Landrini M. Numerical simulation of interfacial flows by smoothed particle hydrodynamics. J Comput Phys. 2003;191:448-75.

[25] Domínguez JM, Crespo AJC, Valdez-Balderas D, Rogers BD, Gómez-Gesteira M. New multi-GPU implementation for smoothed particle hydrodynamics on heterogeneous clusters. Comput Phys Commun. 2013;184:1848-60.

[26] Mokos A, Rogers BD, Stansby PK, Domínguez JM. Multi-phase SPH modelling of violent hydrodynamics on GPUs. Comput Phys Commun. 2015;196:304-16.

[27] Liu GR, Liu MB. Smoothed particle hydrodynamics:a meshfree particle methods. Singapore: World Scientific; 2003.

[28] Colagrossi A. A meshless Lagrangian method for free-surface and interface flows with fragmentation [Ph.D. thesis]. Rome, Italy: Sapienza University of Rome; 2004.

[29] Colagrossi A, Antuono M, Le Touzé D. Theoretical considerations on the free-surface role in the smoothed-particle-hydrodynamics model. Phys Rev E. 2009;79:056701.

[30] Nugent S, Posch H. Liquid drops and surface tension with smoothed particle applied mechanics. Phys Rev E. 2000;62:49-68.

[31] Monaghan JJ. On the problem of penetration in particle methods. J Comput Phys. 1989;82:1-15.

[32] Monaghan JJ. Smoothed particle hydrodynamics. Rep Prog Phys. 2005;68:1703.

[33] Marrone S, Colagrossi A, Antuono M, Colicchio G, Graziani G. An accurate SPH modeling of viscous flows around bodies at low and moderate Reynolds numbers. J Comput Phys. 2013;245:456-75.

[34] Colagrossi A, Bouscasse B, Antuono M, Marrone S. Particle packing algorithm for SPH schemes. Comput Phys Commun. 2012;183:1641-53.

[35] Bonet J, Lok T-SL. Variational and momentum preservation aspects of smooth particle hydrodynamic formulations. Comput Methods Appl Mech Eng. 1999;180:97-115.

[36] Adami S, Hu X, Adams N. A generalized wall boundary condition for smoothed particle hydrodynamics. J Comput Phys. 2012;231:7057-75.

[37] Cao XY, Ming FR, Zhang AM. Sloshing in a rectangular tank based on SPH simulation. Appl Ocean Res. 2014;47:241-54.

[38] Zhou ZQ, De Kat JO, Buchner B. A nonlinear 3-D approach to simulate green water dynamics on deck. in the Proceedings of the 7th International Conference on Numerical Ship Hydrodynamics. Nantes, France: Proceedings of the 7th International Conference on Numerical Ship Hydrodynamics; 1999. p. 5.

[39] Greco M. A two-dimensional study of green-water loading [Ph.D. thesis]. Trondheim, Norway: Norwegian University of Science and Technology; 2001.

[40] Pohle FV. The Lagrangian equations of hydrodynamics: solutions which are analytic functions of the time [Ph.D. Thesis]. New York, USA: New York University; 1950.

[41] Barcarolo DA. Improvement of the precision and the efficiency of the SPH method: theoretical and numerical study [Ph.D. thesis]. Nantes, France: Ecole Centrale de Nantes 2013.